EPJ Web of Conferences **3**, 01004 (2010)
DOI:10.1051/epjconf/20100301004
© Owned by the authors, published by EDP Sciences, 2010

Electromagnetic Structure and Reactions of Few-Nucleon Systems in χEFT

L. Girlanda[1,2], S. Pastore[3], R. Schiavilla[3,4,a], and M. Viviani[2]

[1] Department of Physics, University of Pisa, 56127 Pisa, Italy
[2] INFN-Pisa, 56127 Pisa, Italy
[3] Department of Physics, Old Dominion University, Norfolk, VA 23529, USA
[4] Theory Center, Jefferson Lab, Newport News, VA 23606, USA

Abstract. We summarize our recent work dealing with the construction of the nucleon-nucleon potential and associated electromagnetic currents up to one loop in chiral effective field theory (χEFT). The magnetic dipole operators derived from these currents are then used in hybrid calculations of static properties and low-energy radiative capture processes in few-body nuclei. A preliminary set of results are presented for the magnetic moments of the deuteron and trinucleons and thermal neutron captures on p, d, and ^{3}He.

1 Introduction

The non-perturbative character of quantum chromodynamics (QCD) at low energies has so far prevented a quantitative understanding of nuclear structure and reactions in terms of the theory fundamental degrees of freedom, *i.e.* quarks and gluons. However, the chiral symmetry exhibited by QCD severely restricts the form of the interactions of pions among themselves and with other particles [1]. In particular, the pion couples to the baryons, such as nucleons or Δ-isobars, by powers of its momentum Q, and the Lagrangian describing these interactions can be expanded in powers of Q/Λ_χ, where $\Lambda_\chi \sim 1$ GeV specifies the chiral-symmetry breaking scale. As a consequence, classes of Lagrangians emerge, each characterized by a given power of Q/Λ_χ and each involving a certain number of unknown coefficients, so called low-energy constants (LEC's), which are then determined by fits to experimental data (see, for example, the review papers [2], and references therein).

This approach, known as chiral effective field theory (χEFT), has been used to study two- and many-nucleon interactions [2] and the interaction of electroweak probes with nuclei [3,4]. Its validity, though, is restricted to processes occurring at low energies. In this sense, it has a more limited range of applicability than meson-exchange or more phenomenological models of these interactions, which in fact quantitatively and successfully account for a wide variety of nuclear properties and reactions up to energies, in some cases, well beyond the pion production threshold (for a review, see Ref. [5]). However, it can be justifiably argued that χEFT puts nuclear physics on a more fundamental basis by providing, on the one hand, a direct connection between QCD and its symmetries, in particular chiral symmetry, and the strong and electroweak interactions in nuclei, and, on the other hand, a practical calculational scheme susceptible, in principle, of systematic improvement.

The present report summarizes recent work carried out by our group in the construction of the nucleon-nucleon (NN) potential and associated electromagnetic currents up to one loop in χEFT [6,7], and in their application to the calculation of magnetic dipole ($M1$) observables in A=2–4 nuclei [8]. The derivation of the potential and currents is based on time-ordered perturbation theory and the non-relativistic Hamiltonians implied by the chiral Lagrangians of Refs. [9–11], and retains irreducible as well as recoil-corrected reducible diagrams. The latter arise from expanding the energy denominators $(\Delta E_N + \omega_\pi)^{-1}$, where ΔE_N and ω_π denote, respectively, nucleon kinetic energy differences and pion energies, in powers of $\Delta E_N/\omega_\pi$ (which is of order Q, the low-momentum scale). We will not discuss some of the more technical aspects of the formalism, including, for example, the renormalization of loop corrections in dimensional regularization or the cancellations occurring between irreducible and recoil-corrected reducible contributions. Some of these issues were outlined in the talk [12], but the interested reader may want to consult the original papers [6,7].

We will also not attempt to cite all of the extensive literature on these topics—most of which, incidentally, can be found in the review papers mentioned above—but rather will refer only to those papers we are familiar with and which are directly relevant to our work.

2 NN potential at one loop

In Fig. 1 we show the diagrams illustrating the contributions occurring up to N^{2}LO. At LO (Q^0) there is a contact interaction, panel a), along with the one-pion-exchange contribution, panel b). At N^{2}LO (Q^2) there are i) contact interactions involving two gradients acting on the nucleons'

[a] e-mail: schiavil@jlab.org

This is an Open Access article distributed under the terms of the Creative Commons Attribution-Noncommercial License 3.0, which permits unrestricted use, distribution, and reproduction in any noncommercial medium, provided the original work is properly cited.
Article available at http://www.epj-conferences.org or http://dx.doi.org/10.1051/epjconf/20100301004

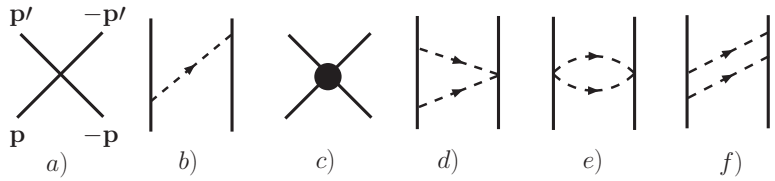

Fig. 1. Diagrams illustrating contributions to the NN potential entering at LO (Q^0), panels a) and b), and N^{2}LO (Q^2), panels c)-f). Nucleons and pions are denoted by solid and dashed lines, respectively. The filled circle in panel c) represents the vertex from contact Hamiltonians containing two gradients of the nucleons' fields. Only one among the possible time orderings is shown for each contribution with more than one vertex.

fields, panel c), and ii) two-pion-exchange loop contributions, panels d)-f). After renormalization, we find that the potential in the center-of-mass frame is given by [7, 10, 11]

$$v(\mathbf{k},\mathbf{K}) = v^{\rm CT0} + v^{\pi}(\mathbf{k}) + v^{\rm CT2}(\mathbf{k},\mathbf{K}) + v^{2\pi}(\mathbf{k}) \qquad (1)$$

where

$$v^{\rm CT0} = C_S + C_T\,\boldsymbol{\sigma}_1\cdot\boldsymbol{\sigma}_2 \qquad (2)$$

$$v^{\pi}(\mathbf{k}) = -\frac{g_A^2}{F_\pi^2}\,\boldsymbol{\tau}_1\cdot\boldsymbol{\tau}_2\,\frac{\boldsymbol{\sigma}_1\cdot\mathbf{k}\,\boldsymbol{\sigma}_2\cdot\mathbf{k}}{m_\pi^2+k^2} \qquad (3)$$

$$\begin{aligned} v^{\rm CT2}(\mathbf{k},\mathbf{K}) &= C_1\,k^2 + C_2\,K^2 + (C_3\,k^2 + C_4\,K^2)\,\boldsymbol{\sigma}_1\cdot\boldsymbol{\sigma}_2 \\ &+ i\,C_5\,\frac{\boldsymbol{\sigma}_1+\boldsymbol{\sigma}_2}{2}\cdot\mathbf{K}\times\mathbf{k} + C_6\,\boldsymbol{\sigma}_1\cdot\mathbf{k}\;\boldsymbol{\sigma}_2\cdot\mathbf{k} \\ &+ C_7\,\boldsymbol{\sigma}_1\cdot\mathbf{K}\;\boldsymbol{\sigma}_2\cdot\mathbf{K} \end{aligned} \qquad (4)$$

$$\begin{aligned} v^{2\pi}(\mathbf{k}) &= \frac{1}{48\pi^2\,F_\pi^4}\boldsymbol{\tau}_1\cdot\boldsymbol{\tau}_2\,G(k)\Big[4\,m_\pi^2(1+4\,g_A^2-5\,g_A^4) \\ &+ k^2(1+10\,g_A^2-23\,g_A^4) - \frac{48\,g_A^4 m_\pi^4}{4\,m_\pi^2+k^2}\Big] \\ &+ \frac{3\,g_A^4}{8\pi^2\,F_\pi^4}\,G(k)\left(k^2\,\boldsymbol{\sigma}_1\cdot\boldsymbol{\sigma}_2 - \boldsymbol{\sigma}_1\cdot\mathbf{k}\,\boldsymbol{\sigma}_2\cdot\mathbf{k}\right), \end{aligned} \qquad (5)$$

the momenta $\mathbf{k}$ and $\mathbf{K}$ are defined in terms of the nucleons' initial and final relative momenta $\mathbf{p}$ and $\mathbf{p}'$ as $\mathbf{k} = \mathbf{p}'-\mathbf{p}$ and $\mathbf{K} = (\mathbf{p}'+\mathbf{p})/2$, g_A and F_π are the nucleon axial coupling constant and pion decay amplitude, respectively, and C_S, C_T, and C_i are LEC's. The function $G(k)$ reads

$$G(k) = \frac{\sqrt{4\,m_\pi^2+k^2}}{k}\,\ln\frac{\sqrt{4\,m_\pi^2+k^2}+k}{\sqrt{4\,m_\pi^2+k^2}-k}\,. \qquad (6)$$

Before turning our attention to a discussion of the phase shifts, we note that the potential above needs to be regularized because of its power-law behavior for large values of the momenta k and/or K. This is accomplished by including a high-momentum cutoff, which we take to be of the form

$$C_\Lambda(k,K) = \mathrm{e}^{-(k^4+16\,K^4)/\Lambda^4} \qquad (7)$$

so that the matrix elements of the regularized potential entering the K-matrix and bound-state equations are obtained from

$$v^{\rm R}(\mathbf{k},\mathbf{K}) = v(\mathbf{k},\mathbf{K})\,C_\Lambda(k,K)\,. \qquad (8)$$

Table 1. Values for the nucleon axial coupling constant g_A, pion decay constant F_π, neutral and charged pion masses m_0 and m_+, and (twice) np reduced mass μ_N, used in the fits.

g_A	F_π (MeV)	m_0 (MeV)	m_+ (MeV)	$2\,\mu_N$ (MeV)
1.29	184.8	134.9766	139.5702	938.9181

In the following cutoff parameters Λ in the range 500–700 MeV are considered. Thus $C_\Lambda(k,K)$ removes momenta larger than (3–4) m_π in a theory retaining up to two-pion-exchange mechanisms, and whose regime of validity extends, therefore, up to 2 m_π.

The LEC's C_S, C_T, and C_i are determined by fitting the deuteron binding energy and S- and P-wave np phase shifts up to laboratory kinetic energies of 100 MeV, as obtained in the very recent (2008) analysis of Gross and Stadler [13]. The parameters characterizing the one- and two-pion exchange parts of the potential are listed in Table 1, with g_A determined from the Golberger-Treiman relation $g_A = g_{\pi NN}F_\pi/(2\,m_N)$, where the πNN coupling constant is taken to have the value $g^2_{\pi NN}/(4\pi) = 13.63\pm0.20$ [14, 15]. In fact, in the one-pion exchange we include the isospin-symmetry breaking induced by the mass difference between charged and neutral pions, since it leads to significant effects in the ^{1}S$_0$ scattering length [16], and therefore the one-pion-exchange potential reads

$$\begin{aligned} v^{\pi}(\mathbf{k}) &= -\frac{g_A^2}{3\,F_\pi^2}\Bigg[\boldsymbol{\tau}_1\cdot\boldsymbol{\tau}_2\left(\frac{1}{k^2+m_0^2}+\frac{2}{k^2+m_+^2}\right) \\ &+ T_{12}\left(\frac{1}{k^2+m_0^2}-\frac{1}{k^2+m_+^2}\right)\Bigg]\boldsymbol{\sigma}_1\cdot\mathbf{k}\,\boldsymbol{\sigma}_2\cdot\mathbf{k} \end{aligned} \qquad (9)$$

where T_{12} is the isotensor operator defined as

$$T_{12} = 3\,\tau_{1,z}\tau_{2,z} - \boldsymbol{\tau}_1\cdot\boldsymbol{\tau}_2 \qquad (10)$$

and m_0 and m_+ are the neutral and charged pions masses. Finally, we note that the pion mass entering in the two-pion-exchange part is taken as $m_\pi = (m_0 + 2\,m_+)/3$.

The best-fit values obtained for the LEC's are listed in Table 2 for Λ=500, 600, and 700 MeV, while results for the S- and P-wave phases used in the fits, as well as for the D-wave and peripheral F- and G-wave phases, and mixing angles $\epsilon_{J=1,\ldots,4}$ are displayed in Figs. 2–7 up to 200 MeV lab kinetic energies. Effective range expansions and

Table 2. Values of the LEC's corresponding to cutoff parameters Λ in the range 500–700 MeV, obtained from fits to np phase shifts up to lab energies of 100 MeV.

	Λ (MeV)		
	500	600	700
C_S (fm^2)	–4.456420	–4.357712	–3.863625
C_T (fm^2)	0.034780	0.094149	0.234176
C_1 (fm^4)	–0.360939	–0.259186	–0.268296
C_2 (fm^4)	–1.460509	–0.934505	–0.835226
C_3 (fm^4)	–0.349780	–0.359547	–0.389047
C_4 (fm^4)	–1.968636	–1.717178	–1.724544
C_5 (fm^4)	–0.870067	–0.754021	–0.695564
C_6 (fm^4)	0.326169	0.301194	0.348152
C_7 (fm^4)	–0.727797	–1.006459	–0.955273

deuteron properties are listed in Table 3. For reference, in Figs. 4–7, following the original work by Kaiser *et al.* [17], the phases obtained by including only the one- and two-pion-exchange (v^π and $v^{2\pi}$, respectively) terms of the potential are also shown. These have been calculated in first order perturbation theory on the T-matrix, and hence are cutoff independent. Overall, the quality of the fits at N^{2}LO is comparable to that reported in Refs. [18,19] and, more recently, in Ref. [20]. While the cutoff dependence is relatively weak for the S-wave phases beyond lab energies of 100 MeV, it becomes significant for higher partial wave phases and for the mixing angles. In particular, the F- and G-wave phases, while small because of the centrifugal barrier, nevertheless display a pronounced sensitivity to short-range physics, although there are indications [21] that inclusion of explicit Δ-isobar degrees of freedom might reduce this sensitivity. Beyond 100 MeV, the agreement between the calculated and experimental phases is generally poor, and indeed in the ^{3}D$_3$ and ^{3}F$_4$ channels they have opposite sign. The scattering lengths are well reproduced by the fits (within $\sim$ 1% of the data, see Table 3), however, the singlet and triplet effective ranges are both significantly underpredicted, by $\sim$ 10% and $\sim$ 5% respectively.

The deuteron S- and D-wave radial wave functions are shown in Fig. 8 along with those calculated with the Argonne v_{18} (AV18) potential [16]. The D wave is particularly sensitive to variations in the cutoff: it is pushed in as Λ is increased from 500 to 700 MeV, but remains considerably smaller than that of the AV18 up to internucleon distances of $\sim$ 1.5 fm, perhaps not surprisingly, since this realistic potential has a strong tensor component at short range. The static properties, *i.e.* D- to S-state ratio, mean-square-root matter radius, and magnetic moment (the binding energy is fitted) are close to the experimental values, and their variation with Λ is quite modest. The quadrupole moment is underpredicted by $\sim$ 4%, a pathology common, to the best of our knowledge, to all realistic potentials (including the AV18).

Table 3. Singlet and triplet np scattering lengths (a_s and a_t) and effective ranges (r_s and r_t), and deuteron binding energy (B_d), D- to S-state ratio (η_d), root-mean-square matter radius (r_d), magnetic moment (μ_d), quadrupole moment (Q_d), and D-state probability (P_D), obtained with Λ=500, 600, and 700 MeV, are compared to the corresponding experimental values.

	Λ (MeV)			
	500	600	700	Expt
a_s (fm)	–23.729	–23.736	–23.736	–23.749(8)
r_s (fm)	2.528	2.558	2.567	2.81(5)
a_t (fm)	5.360	5.371	5.376	5.424(3)
r_t (fm)	1.665	1.680	1.687	1.760(5)
B_d (MeV)	2.2244	2.2246	2.2245	2.224575(9)
η_d	0.0267	0.0260	0.0264	0.0256(4)
r_d (fm)	1.943	1.947	1.951	1.9734(44)
μ_d (μ_N)	0.860	0.858	0.853	0.8574382329(92)
Q_d (fm^2)	0.275	0.272	0.279	0.2859(3)
P_D (%)	3.44	3.87	4.77	

3 Magnetic moments at one loop

The LO term in the electromagnetic current operator results from the coupling of the external photon field to the individual nucleons, and is counted as $e\,Q^{-2}$ (e is the electric charge), where a factor $e\,Q$ is from the γNN vertex, and a factor Q^{-3} follows from the momentum δ-function implicit in this type of disconnected diagrams. It consists of the standard convection and spin-magnetization currents of the nucleon. The NLO term (of order $e\,Q^{-1}$) involves seagull and in-flight contributions associated with one-pion exchange, and the N^{2}LO term (of order $e\,Q^0$) represents the $(Q/m_N)^2$ relativistic correction to the LO one-body current (m_N denotes the nucleon mass). Explicit expressions for all these are listed in Refs. [6,7].

At N^{3}LO ($e\,Q$) we distinguish three classes of terms [7]: i) two-pion exchange currents at one loop, illustrated by diagrams (a)-(i) in Fig. 9, ii) a tree-level one-pion exchange current involving the standard πNN vertex on one nucleon, and a $\gamma\pi NN$ vertex of order $e\,Q^2$ on the other nucleon, illustrated by diagram (j), and iii) currents generated by minimal substitution in the four-nucleon contact interactions involving two gradients of the nucleons' fields as well as by non-minimal couplings, collectively represented by diagram (k). A fourth class consisting of $(Q/m_N)^2$ relativistic corrections to the NLO currents is neglected.

The two-body magnetic moment ($M1$) operator associated with these currents is conveniently separated into a term dependent on the center-of-mass position $\mathbf{R}$ of the two nucleons and one independent of it [22]. The former, known as the Sachs' contribution, is uniquely determined, via the continuity equation, by the χEFT potential at order Q^2, and reads [7]:

$$\boldsymbol{\mu}^{\rm N^3LO}_{\rm Sachs} = -\frac{i}{2}\,e\,(\boldsymbol{\tau}_1\times\boldsymbol{\tau}_2)_z\,\mathbf{R}\times\nabla_k\,v_0^{2\pi}(k) + \frac{e}{4}\frac{\tau_{1,z}-\tau_{2,z}}{2}\mathbf{R} \times\Big[2\,(C_2+C_4\,\boldsymbol{\sigma}_1\cdot\boldsymbol{\sigma}_2)\,\mathbf{K} - i\,C_5\,\frac{\boldsymbol{\sigma}_1+\boldsymbol{\sigma}_2}{2}\times\mathbf{k} + C_7\,(\boldsymbol{\sigma}_1\,\boldsymbol{\sigma}_2\cdot\mathbf{K}+\boldsymbol{\sigma}_1\cdot\mathbf{K}\,\boldsymbol{\sigma}_2)\Big] \qquad (11)$$

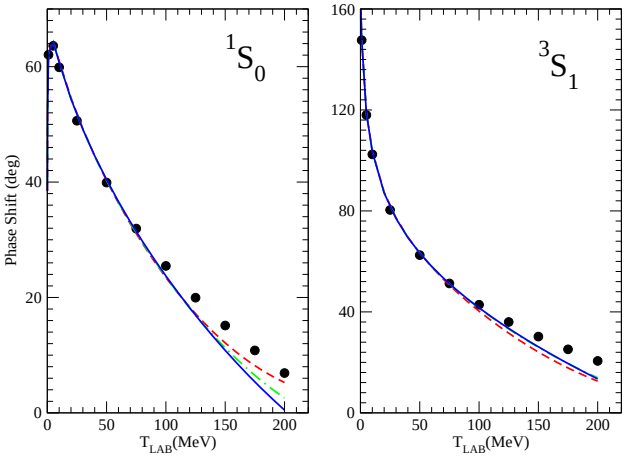

Fig. 2. The S-wave *np* phase shifts, obtained with cutoff parameters Λ=500, 600, and 700 MeV, are denoted by dash (red), dot-dash (green), and solid (blue) lines, respectively. The filled circles represent the phase-shift analysis of Ref. [13].

where $v_0^{2\pi}(k)$ is the isospin-dependent part of the two-pion-exchange chiral potential at order Q^2, and C_2, C_4, C_5, and C_7 are low-energy constants (LEC's) entering the contact potential at order Q^2. The function $v_0^{2\pi}(k)$ is defined as

$$v_0^{2\pi}(k) = \frac{1}{48\pi^2 F_\pi^4} G(k) \Big[4 m_\pi^2 (1 + 4 g_A^2 - 5 g_A^4) + k^2 (1 + 10 g_A^2 - 23 g_A^4) - \frac{48 g_A^4 m_\pi^4}{4 m_\pi^2 + k^2} \Big] . \quad (12)$$

The translationally invariant $M1$ operators associated with pion loops [diagrams (a)-(i) in Fig. 9], the one-pion-exchange current of order $e\,Q$ [diagram (j)], and contact currents due to non-minimal couplings [diagram (k)] are given, respectively, by [7]

$$\boldsymbol{\mu}_{\rm loop}^{\rm N^3LO} = \frac{e\, g_A^2}{8\pi^2 F_\pi^4} \tau_{2,z} \Big[F_0(k)\, \boldsymbol{\sigma}_1 - F_2(k) \frac{\mathbf{k}\, \boldsymbol{\sigma}_1 \cdot \mathbf{k}}{k^2} \Big] + \frac{e\, g_A^2}{2\pi^2 F_\pi^2} \tau_{2,z} \, (C_S\, \boldsymbol{\sigma}_2 - C_T\, \boldsymbol{\sigma}_1) + 1 \rightleftharpoons 2 \quad (13)$$

$$\boldsymbol{\mu}_{\rm tree}^{\rm N^3LO} = e \frac{g_A}{F_\pi^2} \Big[\big(d_8' \tau_{2,z} + d_9' \boldsymbol{\tau}_1 \cdot \boldsymbol{\tau}_2 \big) \mathbf{k} - d_{21}' \, (\boldsymbol{\tau}_1 \times \boldsymbol{\tau}_2)_z \boldsymbol{\sigma}_1 \times \mathbf{k} \Big] \frac{\boldsymbol{\sigma}_2 \cdot \mathbf{k}}{k^2 + m_\pi^2} + 1 \rightleftharpoons 2 \quad (14)$$

$$\boldsymbol{\mu}_{\rm CT}^{\rm N^3LO} = -e\, C_{15}' \, \boldsymbol{\sigma}_1 - e\, C_{16}' (\tau_{1,z} - \tau_{2,z}) \, \boldsymbol{\sigma}_1 + 1 \rightleftharpoons 2 \quad (15)$$

where d_8', d_9', d_{21}', C_{15}', and C_{16}', are additional LEC's to be determined as discussed below, while the functions $F_i(k)$ are defined as

$$F_0(k) = 1 - 2 g_A^2 + \frac{8 g_A^2 m_\pi^2}{k^2 + 4 m_\pi^2} + G(k) \Big[2 - 2 g_A^2 - \frac{4 (1 + g_A^2) m_\pi^2}{k^2 + 4 m_\pi^2} + \frac{16 g_A^2 m_\pi^4}{(k^2 + 4 m_\pi^2)^2} \Big] \quad (16)$$

$$F_2(k) = 2 - 6 g_A^2 + \frac{8 g_A^2 m_\pi^2}{k^2 + 4 m_\pi^2} + G(k) \Big[4 g_A^2 - \frac{4 (1 + 3 g_A^2) m_\pi^2}{k^2 + 4 m_\pi^2} + \frac{16 g_A^2 m_\pi^4}{(k^2 + 4 m_\pi^2)^2} \Big] . \quad (17)$$

It is interesting to note that the constant $2 - 6 g_A^2$ in $F_2(k)$ would lead to a long-range contribution of the type

$$[\tau_{2,z} (\boldsymbol{\sigma}_1 \cdot \boldsymbol{\nabla}) \boldsymbol{\nabla} + 1 \rightleftharpoons 2] \, 1/r$$

in the magnetic moment, which is, however, fictitious in the present context of an effective field theory valid at low momenta, since in performing the Fourier transform the high momentum components are suppressed by the cutoff $\overline{C}_\Lambda(k)$ (see below).

The isovector part of $\boldsymbol{\mu}_{\rm tree}^{\rm N^3LO}$ has the same structure as the $M1$ operator involving N-Δ excitation [6], to which it reduces if the following identifications are made: $d_{21}'/d_8' = 1/4$, and $d_8' = 4\mu^* h_A/(9\, m_N\, \Delta)$, where h_A is the $\pi N \Delta$ coupling constant, μ^* is the $N\Delta$-transition magnetic moment, and Δ is the Δ-N mass difference, $\Delta = m_\Delta - m_N$. In this resonance saturation picture, the term proportional to d_8' can also be interpreted as due to the $\omega\pi\gamma$ transition current, ignoring ω-meson propagation (see Ref. [5] and references therein), in which case $d_8' = g_{\omega\pi\gamma} g_{\omega NN} F_\pi / m_\omega^3$, where $g_{\omega\pi\gamma}$ is the $\omega\pi\gamma$ transition coupling constant, $g_{\omega NN}$ is the ωNN vector coupling constant, and m_ω is the ω-meson mass. Similarly, the isoscalar part of $\boldsymbol{\mu}_{\rm tree}^{\rm N^3LO}$ reduces to the $\rho\pi\gamma$ $M1$ operator, if $d_9' = g_{\rho\pi\gamma} g_{\rho NN} F_\pi / m_\rho^3$, where $g_{\rho\pi\gamma}$ is the $\rho\pi\gamma$ transition coupling constant, $g_{\rho NN}$ is the ρNN vector coupling constant, and m_ρ is the ρ-meson mass.

Currents in χEFT at N^{3}LO have also been derived, using different formalisms, by Park *et al.* in Ref. [4] and, more recently, by Kölling *et al.* in Ref. [23]. The derivation in Ref. [4] is based on covariant perturbation theory, and includes only the contribution of irreducible diagrams. Consequently, the cancellations occurring between the latter and recoil-corrected diagrams are lacking, and the resulting $\boldsymbol{\mu}_{\rm loop}^{\rm N^3LO}$ (in particular, its isospin structure) is different from that given here. In addition, the authors of Ref. [4]

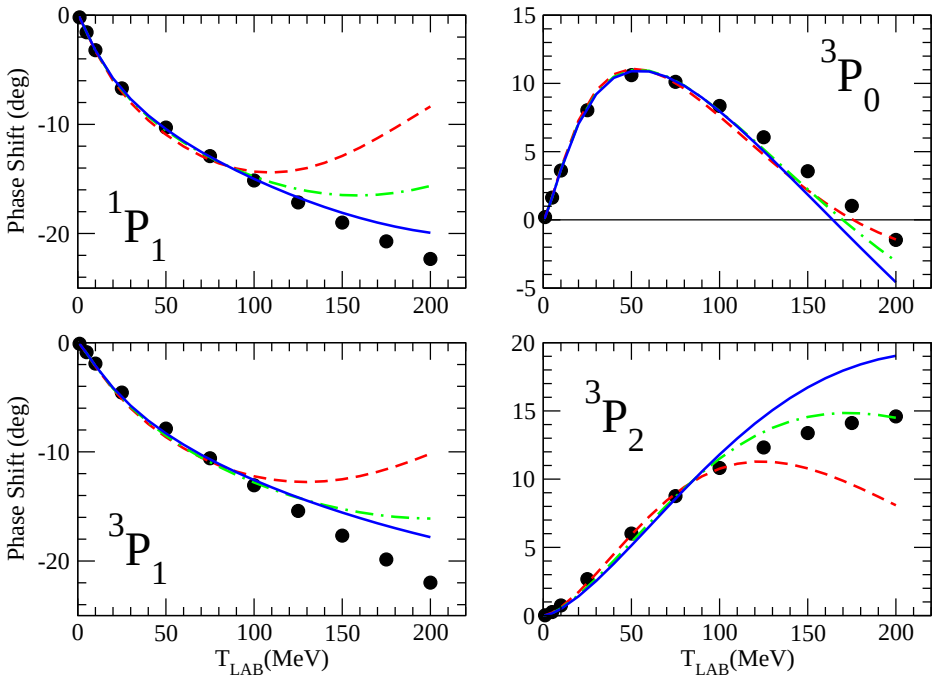

Fig. 3. Same as in Fig. 2, but for P-wave phase shifts.

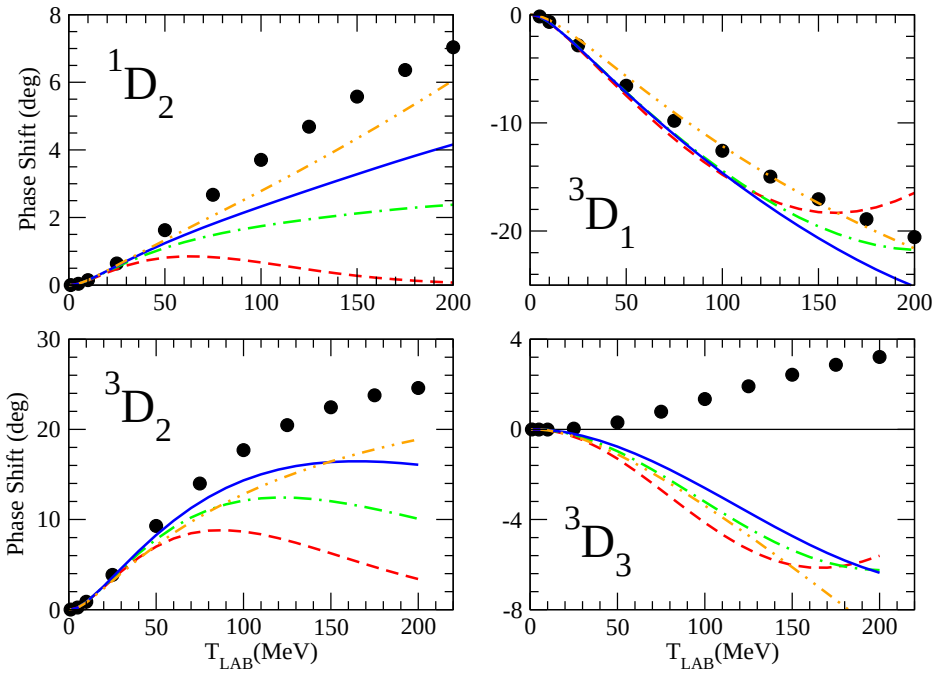

Fig. 4. Same as in Fig. 2, but for D-wave phase shifts. The dash-double-dot (orange) line is obtained in first order perturbation theory for the T-matrix by including only the one- and two-pion-exchange parts of the N^{2}LO potential.

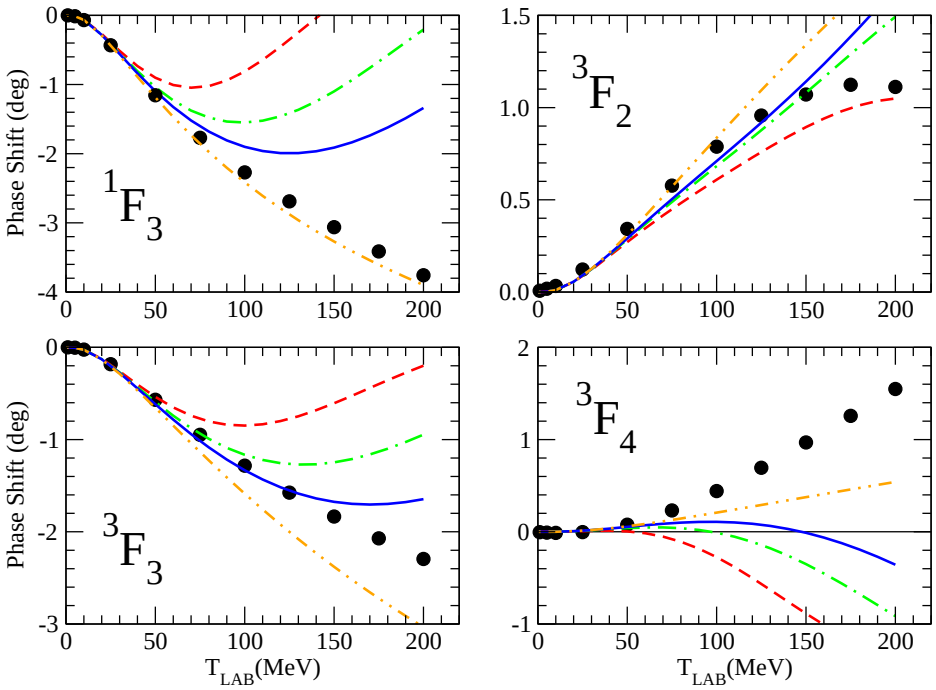

Fig. 5. Same as in Fig. 4, but for F-wave phase shifts.

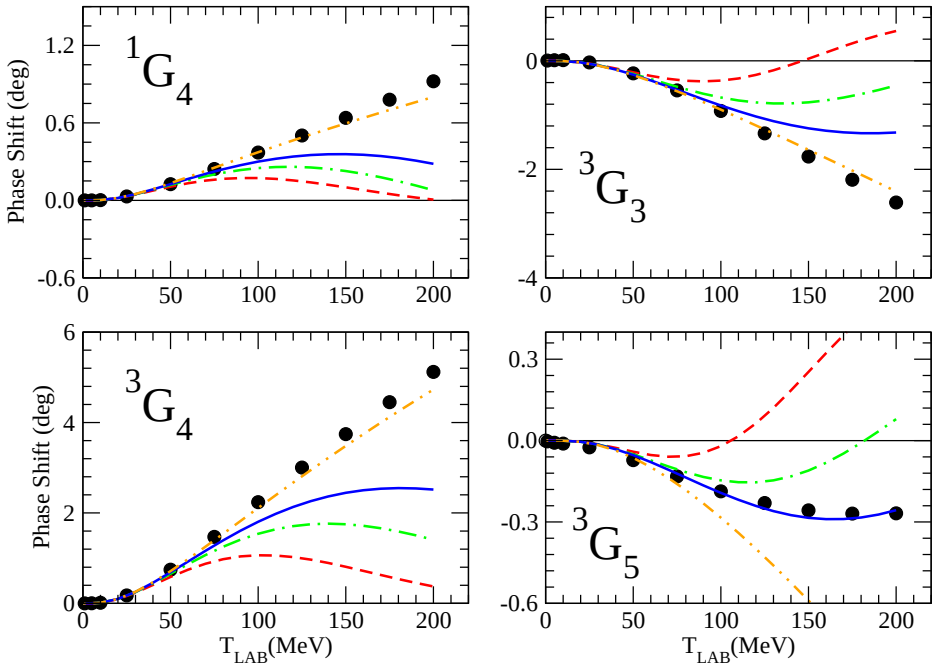

Fig. 6. Same as in Fig. 4, but for G-wave phase shifts.

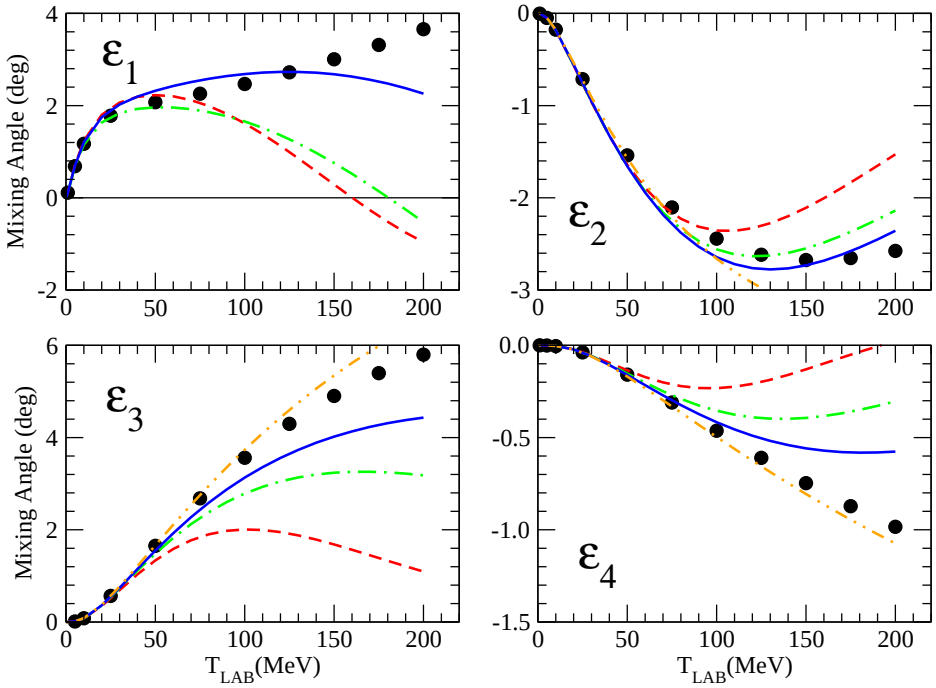

Fig. 7. Same as in Fig. 4, but for the mixing angles ϵ_J.

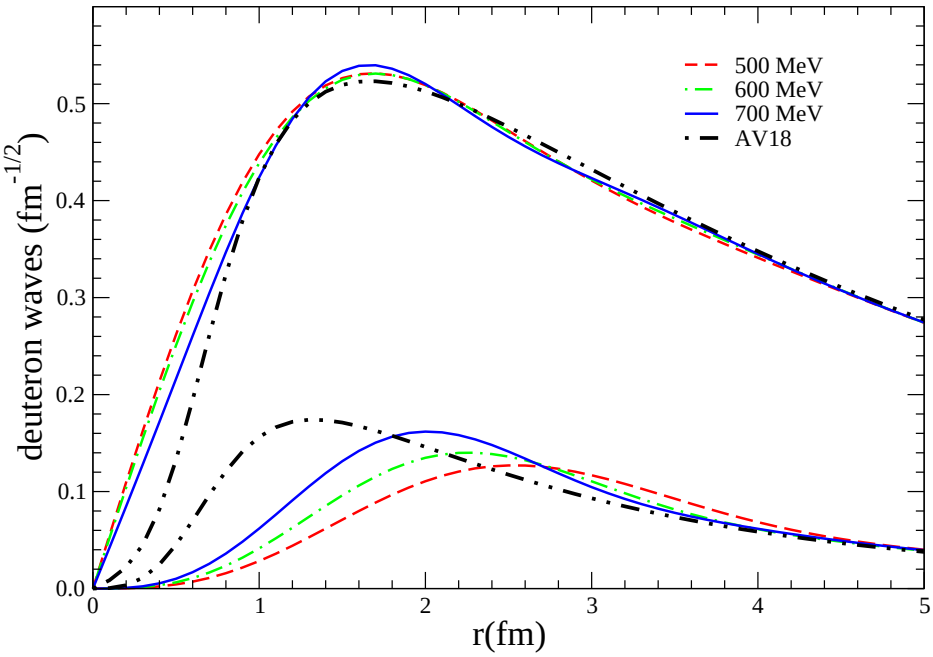

Fig. 8. (Color online) The S-wave and D-wave components of the deuteron, obtained with cutoff parameters Λ=500, 600, and 700 MeV and denoted by dash (red), dot-dash (green), and solid (blue) lines, respectively, are compared with those calculated from the Argonne v_{18} potential (dash-double-dot black lines).

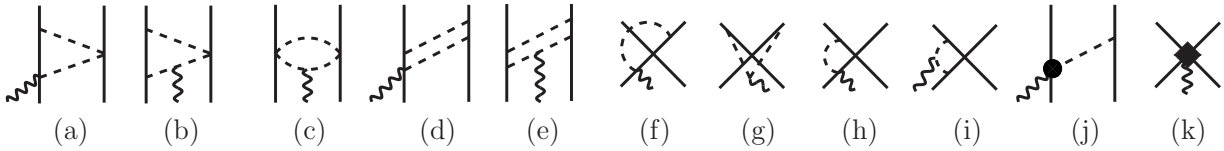

Fig. 9. Diagrams illustrating two-body currents at N^{3}LO. Nucleons, pions, and photons are denoted by solid, dashed, and wavy lines, respectively. Only one among the possible time orderings is shown for diagrams (a)-(j).

neglect the terms in $\boldsymbol{\mu}_{\rm loop}^{\rm N^3LO}$ proportional to the LEC's C_S and C_T as well as those in $\boldsymbol{\mu}_{\rm Sachs}^{\rm N^3LO}$ proportional to the C_i, i=2, 4, 5, and 7.

The derivation in Ref. [23] uses time-ordered perturbation theory in combination with a unitary transformation that decouples, in the Hilbert space of nucleons and pions, the states consisting of nucleons only from those containing, in addition, pions [11]. The resulting expressions for the two-pion-exchange currents, the only ones considered by the authors of Ref. [23], are in agreement with those obtained in Ref. [7].

4 $M1$ observables in A=2–4 systems

In the present contribution we report on the first stage of a research program aimed at studying electromagnetic observables of light nuclei, and particularly radiative capture processes in the three- and four-nucleon systems, within a consistent χEFT framework, *i.e.* with the one-loop potential and currents discussed in the previous sections. Here, we present results for $M1$ transitions in A=2–4 nuclei obtained in the hybrid approach, i.e., by evaluating the matrix elements of the χEFT $M1$ operators between wave functions obtained from realistic potentials. We consider the Argonne v_{18} [16] and chiral N^{3}LO [19] two-nucleon potentials in combination with the Urbana-IX [24] and chiral [25] (N2LO) three-nucleon potentials. These models, denoted as AV18/UIX and N3LO/N2LO, provide an excellent description of three- and four-nucleon bound and scattering state properties, including binding energies, radii, and effective range expansions [26]. The AV18/UIX model has also been used in a recent (hybrid) calculation of the astrophysical factor for the p-p and p-^{3}He fusion reactions by weak capture at the keV energies relevant in the interior of the Sun [27].

Neutron and proton radiative captures on ^{2}H, ^{3}H and ^{3}He are particularly challenging from the standpoint of nuclear few-body theory. This can be appreciated by comparing the measured values for the cross sections of thermal neutron radiative capture on ^{1}H, ^{2}H, ^{3}He. Their respective values in mb are: (332.6 ± 0.7) [28], (0.508 ± 0.015) [29], and (0.055 ± 0.003) [30]. Thus, in going from A=2 to 4 the cross section has dropped by almost four orders of magnitude. These processes are induced by $M1$ transitions between the initial two-cluster state in relative S-wave and the final bound state. The ^{3}H and ^{4}He wave functions, respectively Ψ_3 and Ψ_4, are approximately eigenfunctions of the one-body $M1$ operator $\boldsymbol{\mu}$, namely $\mu_z\Psi_3 \simeq \mu_p\Psi_3$ and $\mu_z\Psi_4 \simeq 0$, where μ_p=2.793 n.m. is the proton magnetic moment—the experimental value of the ^{3}H magnetic moment is 2.979 n.m, while ^{4}He has no magnetic moment. These relations would be exact, if the ^{3}H and ^{4}He wave functions were to consist of the symmetric S-wave term only. In fact, tensor components in the nuclear potentials generate significant D-state admixtures, that partially spoil this eigenstate property. To the extent that it is approximately satisfied, though, the matrix elements $\langle\Psi_3 \mid \mu_z \mid \Psi_{1+2}\rangle$ and $\langle\Psi_4 \mid \mu_z \mid \Psi_{1+3}\rangle$ vanish due to orthogonality between the initial and final states. This orthogonality argument fails in the case of the deuteron, since then $\mu_z\Psi_2 \simeq (\mu_p - \mu_n)\,\phi_2(S)\,\chi_0^0\,\eta_0^1$, where $\chi_{M_S}^S$ and $\eta_{M_T}^T$ are two-nucleon spin and isospin states, respectively. The $M1$ operator can therefore connect the large S-wave component ϕ_2(S) of the deuteron to a T=1 ^{1}S$_0$ n-p state (the orthogonality between the latter and the deuteron follows from the orthogonality between their respective spin-isospin states).

As a result of this suppression, the n-d, p-d, n-^{3}He, and p-^{3}H radiative (as well as p-^{3}He weak) captures are very sensitive to small components in the wave functions, particularly the D-state admixtures generated by tensor forces, and to many-body terms in the electromagnetic (and weak) current operators.

The χEFT $M1$ operators discussed in the previous section, regularized by a cutoff $\overline{C}_\Lambda(k) = \exp(-k^4/\Lambda^4)$ with Λ in the range between 500 MeV and 700 MeV, have been used [8] to study the magnetic moments of the deuteron and trinucleons, and the np, nd, and n ^{3}He radiative captures at thermal neutron energies. At N^{3}LO there are no three-body currents, since the contributions of diagrams (a) and (d) in Fig. 10, involving the $\pi\pi NN$ vertex, vanish, while those due to the irreducible and recoil-corrected reducible diagrams—only irreducible diagrams are shown in panels (b)-(c) and (e)-(f) of Fig. 10—exactly cancel out.

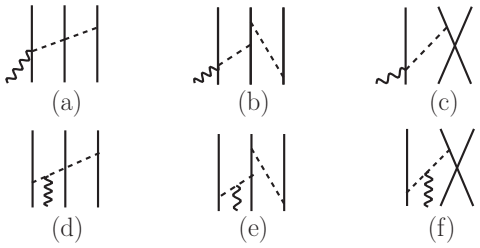

Fig. 10. Diagrams illustrating three-body currents at N^{3}LO. Notation as in Fig. 9. Their contribution vanishes, see text for discussion.

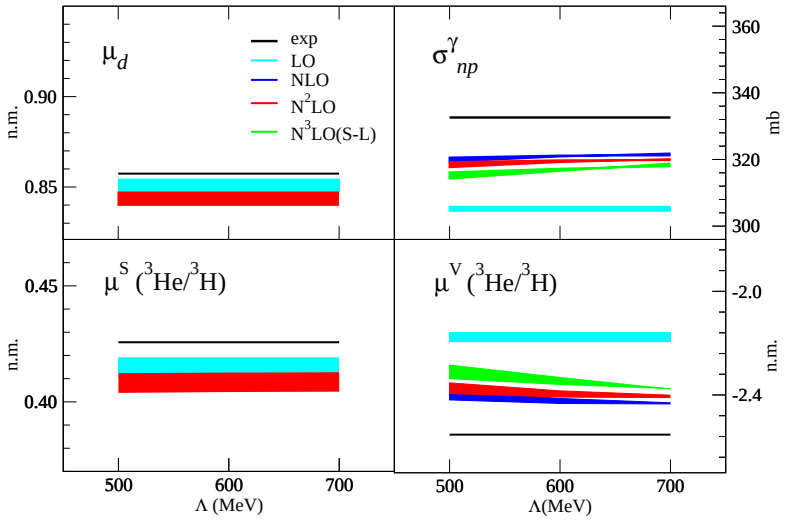

Fig. 11. Results for the deuteron and trinucleon isoscalar and isovector magnetic moments, and *np* radiative capture, obtained by including cumulatively the LO, NLO, N^{2}LO, and N^{3}LO(S-L) contributions. See text for discussion.

Table 4. Adimensional values of the isoscalar LEC's corresponding to cutoff parameters Λ in the range 500–700 MeV obtained for the AV18/UIX (N3LO/N2LO) Hamiltonian. See text for explanation.

Λ	$d_1^S \times 10^2$	d_2^S
500	–8.85 (–0.225)	–3.18 (–2.38)
600	–2.90 (9.20)	–7.10 (–5.30)
700	6.64 (20.4)	–13.2 (–9.83)

Table 5. Adimensional values of the isovector LEC's corresponding to cutoff parameters Λ in the range 500–700 MeV obtained for the AV18/UIX (N3LO/N2LO) Hamiltonian. See text for explanation.

Λ	d_1^V	d_2^V
500	5.18 (5.82)	–11.3 (–11.4)
600	6.55 (6.85)	–12.9 (–23.3)
700	8.24 (8.27)	–1.70 (–46.2)

We now turn our attention to the determination of the LEC's d_8', d_9', d_{21}', C_{15}', and C_{16}'. In principle, the d_i' could be fitted to pion photoproduction data on a single nucleon, or related to hadronic coupling constants (although $g_{\omega NN}$ and $g_{\rho NN}$ are rather poorly known) by resonance saturation arguments. Indeed, this latter strategy is used in a series of calculations, based on the $M1$ operators derived in Ref. [4], of the *np*, *nd*, and $n\,^3$He radiative captures, and magnetic moments of A=2 and 3 nuclei [4,31]. Here, however, we assume $d_{21}'/d_8' = 1/4$ as suggested by resonance saturation, and rely on nuclear data to constrain the remaining four LEC's. The values obtained by reproducing the experimental *np* cross section and magnetic moments of the deuteron and trinucleons are listed in Tables 4 and 5. Note that the adimensional values reported there are in units of powers of Λ, i.e., we have defined $d_9' = d_1^S/\Lambda^2$, $C_{15}' = d_2^S/\Lambda^4$, $d_{21}' = d_1^V/\Lambda^2$, and $C_{16}' = d_2^V/\Lambda^4$ and the superscripts S and V denote the isoscalar and isovector content of the associated operators.

In the discussion to follow, we will refer to the terms in Eqs. (11) and (13) as N^{3}LO(S-L) and to those in Eqs. (14) and (15) as N^{3}LO(LECs). In Fig. 11 we show results obtained by including cumulatively the contributions at LO, NLO, N^{2}LO, and N^{3}LO(S-L) for the deuteron (μ_d) and ^{3}He/^{3}H isoscalar (μ^S) magnetic moments (left panels), and for the *np* radiative capture cross section (σ_{np}^γ) at thermal energies and ^{3}He/^{3}H isovector (μ^V) magnetic moment (right panels). The NLO and N^{3}LO(S-L) $M1$ operators are purely isovector, and hence do not contribute to μ_d and μ^S, while the Sachs' term in the N^{3}LO(S-L) operator vanishes in A=2 systems. The band represents the spread in the calculated values corresponding to the two Hamiltonian models considered here (AV18/UIX and N3LO/N2LO). The sensitivity to short-range mechanisms (effective at internucleon separations less than $(2\,m_\pi)^{-1}$, say) as encoded in the cutoff $\overline{C}_\Lambda(k)$ and in the rather different short-range behaviors of the adopted potentials, remains quite weak for all observables. Of course, taking into account the N^{3}LO contribution with the LEC values listed in Tables 4 and 5 reproduces the experimental data represented by the black band (to accommodate errors, although these are negligible in the present case). The contributions at LO and NLO have the same sign, while those at N^{2}LO and N^{3}LO(S-L)

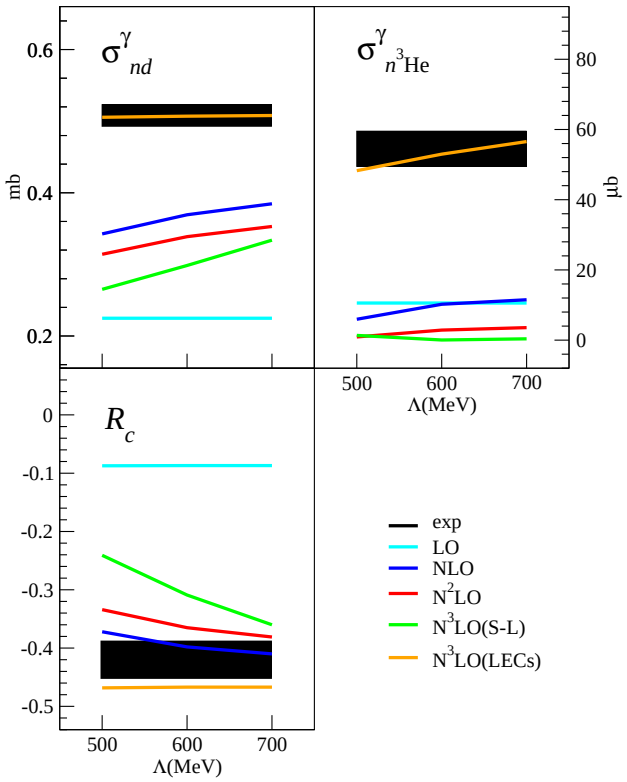

Fig. 12. Results for σ^{γ}_{nd} (left top panel), $\sigma^{\gamma}_{n^3\mathrm{He}}$ (right top panel), and R_c (left bottom panel), obtained by including cumulatively the LO, NLO, N^{2}LO, N^{3}LO(S-L), and N^{3}LO(LECs) contributions. See text for discussion.

have each opposite sign, and tend to increase the difference between theory and experiment.

Having fully constrained the $M1$ operator up to N^{3}LO, we are now in a position to present a preliminary set of predictions, shown in Fig. 12, for the *nd* and $n\,^3$He radiative capture cross sections, denoted as σ^{γ}_{nd} and $\sigma^{\gamma}_{n^3\mathrm{He}}$, and the photon circular polarization parameter R_c resulting from the capture of polarized neutrons on deuterons. The experimental data (black bands) are from Ref. [29] for *nd* and Ref. [30] for $n\,^3$He. In this first stage, we have used only the AV18/UIX (N3LO/N2LO) wave functions for the A=3 (A=4) processes.

Results obtained with the complete N^{3}LO operator are shown by the orange lines labeled N^{3}LO(LECs), and are in very satisfactory agreement with data. Their sensitivity to the cutoff is negligible for *nd* and at the 5% level for $n\,^3$He. As already remarked, these processes are strongly suppressed at LO: the calculated σ^{γ}_{nd}(LO) and $\sigma^{\gamma}_{n^3\mathrm{He}}$(LO) are less than half and a factor of five smaller than the measured values. In the case of $n\,^3$He, the matrix element at NLO is of opposite sign and twice as large (in magnitude) compared to that at LO, hence $\sigma^{\gamma}_{n^3\mathrm{He}}$ at LO and LO+NLO are about the same, as seen in Fig. 12. For *nd*, however, the LO and NLO contributions interfere constructively. For both *nd* and $n\,^3$He, the N^{2}LO and N^{3}LO(S-L) corrections exhibit the same pattern discussed in connection with Fig. 11. The N^{3}LO(LECs) contributions are large and crucially important for bringing theory into agreement with experiment.

Song *et al.* (2009) [31] and Lazauskas *et al.* [31] have reported values for the *nd* and $n\,^3$He capture cross sections about 6% and 15% smaller than measured, with a significantly larger sensitivity (estimated at $\simeq$ 15% for both processes) to the cutoff. We have already noted the differences between the N^{3}LO $M1$ operators used by these authors (in particular, their reliance on resonance saturation to constrain the LEC's entering $\boldsymbol{\mu}^{\mathrm{N^3LO}}_{\mathrm{tree}}$) and those in the present work.

The work of R.S. is supported by the U.S. Department of Energy, Office of Nuclear Physics under contract DE-AC05-06OR23177. Some of the calculations were made possible by grants of computing time from the National Energy Research Supercomputer Center.

References

1. S. Weinberg, *The Quantum Theory of Fields*, vol. II (Cambridge University Press, 1995).

2. V. Bernard, N. Kaiser, and U.-G. Meissner, Int. J. Mod. Phys. **E4** (1995) 193; U. van Kolck, Prog. Part. Nucl. Phys. **43** (1999) 337; P. Bedaque and U. van Kolck, Ann. Rev. Nucl. Part. Sci. **52** (2002) 339; E. Epelbaum, Prog. Part. Nucl. Phys. **57** (2006) 654; E. Epelbaum, H.-W. Hammer, and U.-G. Meissner, Rev. Mod. Phys. in press, arXiv:0811.1338 (2008).
3. T.-S. Park, D.-P. Min, and M. Rho, Phys. Rep. **233** (1993) 341.
4. T.-S. Park, D.-P. Min, and M. Rho, Nucl. Phys. **A596** (1996) 515.
5. J. Carlson and R. Schiavilla, Rev. Mod. Phys. **70** (1998) 743.
6. S. Pastore, R. Schiavilla, and J.L. Goity, Phys. Rev. **C78** (2008) 064002.
7. S. Pastore, L. Girlanda, R. Schiavilla, M. Viviani, and R.B. Wiringa, Phys. Rev. **C80** (2009) 064002.
8. L. Girlanda, A. Kievsky, L.E. Marcucci, S. Pastore, R. Schiavilla, and M. Viviani, in preparation.
9. S. Weinberg, Phys. Lett. **B251** (1990) 288; Nucl. Phys. **B363** (1991) 3; Phys. Lett. **B295** (1992) 114.
10. U. van Kolck, Phys. Rev. **C49** (1994) 2932; C. Ordónez, L. Ray, and U. van Kolck, Phys. Rev. **C53** (1996) 2086.
11. E. Epelbaum, W. Glöckle, and U.-G. Meissner, Nucl. Phys. **A637** (1998) 107; Nucl. Phys. **A747** (2005) 362.
12. R. Schiavilla, http://fb19.hiskp.uni-bonn.de.
13. F. Gross and A. Stadler, Phys. Rev. **C78** (2008) 014005.
14. V.G.J. Stoks, R.G.E. Timmermans, J.J. de Swart, Phys. Rev. **C47** (1993) 512.
15. R.A. Arndt, R.L. Workman, and M.M. Pavan, Phys. Rev. **C49** (1994) 2729.
16. R.B. Wiringa, V.G.J. Stoks, and R. Schiavilla, Phys. Rev. **C51** (1995) 38.
17. N. Kaiser, R. Brockmann, and W. Weise, Nucl. Phys. **A625** (1997) 758.
18. E. Epelbaum, W. Glöckle, and U.-G. Meissner, Nucl. Phys. **A671**(2000) 295; Eur. Phys. J. **A19** (2004) 125; Eur. Phys. J. **A19** (2004) 401.
19. D.R. Entem and R. Machleidt, Phys. Rev. **C66** (2002) 014002; Phys. Rev. **C68** (2003) 041001(R).
20. C.-J. Yang, Ch. Elster, and D.R. Phillips, Phys. Rev. **C80** (2009) 034002; Phys. Rev. **C80** (2009) 044002.
21. N. Kaiser, S. Gerstendoerfer, W. Weise, Nucl. Phys. **A637** (1998) 395.
22. R.G. Sachs, Phys. Rev. **74** (1948) 433; R.H. Dalitz, Phys. Rev. **95** (1954) 799.
23. S. Kölling, E. Epelbaum, H. Krebs, U.-G. Meissner, Phys. Rev. **C80** (2009) 045502.
24. B.S. Pudliner *et al.*, Phys. Rev. **C56** (1997) 1720.
25. D. Gazit, S. Quaglioni, and P. Navratil, Phys. Rev. Lett. **103** (2009) 102502.
26. A. Kievsky *et al.*, J. Phys. **G35** (2008) 063101.
27. T.-S. Park *et al.*, Phys. Rev. **C67** (2003) 055206.
28. S.F. Mughabghab, M. Divadeenam, and N.E. Holden, *Neutron Cross Sections from Neutron Resonance Parameters and Thermal Cross Sections* (Academic Press, London, 1981).
29. E.T. Jurney, P.J. Bendt, and J.C. Browne, Phys. Rev. **C25** (1982) 2810.
30. F.L.H. Wolfs, S.J. Freedman, J.E. Nelson, M.S. Dewey, and G.L. Greene, Phys. Rev. Lett. **63** (1989) 2721; R. Wervelman, K. Abrahams, H. Postma, J.G.L. Booten, and A.G.M. Van Hees, Nucl. Phys. **A526** (1991) 265.
31. T.-S. Park, K. Kubodera, D.-P. Min, and M. Rho, Phys. Lett. **B472** (2000) 232; Y.-H. Song, R. Lazauskas, T.-S. Park, and D.-P. Min, Phys. Lett. **B656** (2007) 174; Y.-H. Song, R. Lazauskas, and T.-S. Park, Phys. Rev. **C79** (2009) 064002; R. Lazauskas, Y.-H. Song, and T.-S. Park, arXiv:0905.3119.